



Low-temperature transport properties of Tl-doped Bi₂Te₃ single crystals

Hang Chi,¹ Wei Liu,¹ Kai Sun,² Xianli Su,¹ Guoyu Wang,¹ Petr Lošťák,³ Vladimír Kucek,³ Čestmír Drašar,³ and Ctirad Uher^{1,*}

¹*Department of Physics, University of Michigan, Ann Arbor, Michigan 48109, USA*

²*Department of Materials Science and Engineering, University of Michigan, Ann Arbor, Michigan 48109, USA*

³*Faculty of Chemical Technology, University of Pardubice, Studentská 573, 532 10 Pardubice, Czech Republic*

(Received 29 April 2013; published 15 July 2013)

While the bulk, stoichiometric Bi₂Te₃ single crystals often exhibit *p*-type metallic electrical conduction due to the Bi_{Te}-type antisite defects, doping by thallium (Bi_{2-x}Tl_xTe₃, $x = 0-0.30$) progressively changes the electrical conduction of single crystals from *p* type ($0 \leq x \leq 0.08$) to *n* type ($0.12 \leq x \leq 0.30$). This is observed via measurements of both the Seebeck coefficient and the Hall effect performed in the crystallographic (0001) plane in the temperature range of 2–300 K. Since any kind of substitution of Tl on the Bi or Te sublattices would result in an enhancement of the density of holes rather than its decrease, and because simple incorporation of Tl at interstitial sites or in the van der Waals gap is unlikely as it would increase the lattice parameters which is not observed in experiments, incorporation of Tl likely proceeds via the formation of TlBiTe₂ fragments coexisting with the quintuple layer structure of Bi₂Te₃. At low levels of Tl, $0 \leq x \leq 0.05$, the temperature-dependent in-plane ($I \perp c$) electrical resistivity maintains its metallic character as the density of holes decreases. Heavier Tl content with $0.08 \leq x \leq 0.12$ drives the electrical resistivity into a prominent nonmetallic regime displaying characteristic metal-insulator transitions upon cooling to below ~ 100 K. At the highest concentrations of Tl, $0.20 \leq x \leq 0.30$, the samples revert back into the metallic state with low resistivity. Thermal conductivity measurements of Bi₂Te₃ single crystals containing Tl, as examined by the Debye-Callaway phonon conductivity model, reveal a generally stronger point-defect scattering of phonons with the increasing Tl content. The systematic evolution of transport properties suggests that the Fermi level of Bi₂Te₃, which initially lies in the valence band (for $x = 0$), gradually shifts toward the top of the valence band (for $0.01 \leq x \leq 0.05$), then moves into the band gap (for $0.08 \leq x \leq 0.12$), and eventually intersects the conduction band (for $0.20 \leq x \leq 0.30$).

DOI: [10.1103/PhysRevB.88.045202](https://doi.org/10.1103/PhysRevB.88.045202)

PACS number(s): 72.80.Jc, 72.20.Pa, 71.55.Ht

I. INTRODUCTION

Single crystals of Bi₂Te₃, which have a layered rhombohedral structure [see Fig. 1(a)] with the space group $R\bar{3}m$ (D_{3d}^5 , S. G. No. 166), are narrow band-gap ($E_g \sim 0.13$ eV at 300 K) semiconductors, renowned for excellent thermoelectric properties and efficient cooling applications at and below room temperature.¹ Bi₂Te₃, together with its isostructural sister compounds Bi₂Se₃ and Sb₂Te₃, have recently been also identified as the most promising materials systems with which to realize a three-dimensional (3D) topological insulator (TI).² Such an exotic state of matter possesses a bulk insulator state together with Dirac-type metallic surface states arising from the unique band structure and strong spin-orbit coupling. While angle-resolved photoelectron spectroscopy (ARPES) measurements have proved without any doubt the presence of topologically protected surface states,³⁻⁶ the spectacular transport properties predicted to be associated with surface states have not yet been fully demonstrated. The primary cause hampering transport measurements is a high conductivity of the bulk state that overshadows the contribution of surface states. This is due to high density of charged antisite defects of the type Bi_{Te}⁻¹ (an atom of Bi occupying a site on the Te sublattice and carrying charge -1 that is compensated by a hole in the valence band) that drive the system *p* type and are responsible for high density of holes on the order of 10^{19} cm⁻³ at room temperature in Bi₂Te₃ crystals grown from stoichiometric melts.⁷ Although experimental techniques, such as post-annealing Bi₂Te₃ crystals in Te vapors,^{8,9} have been developed to compensate such naturally formed acceptor defects in order to achieve a bulk insulator, better and more efficient ways of controlling the carrier density

are still highly desirable. In this paper, we report on our recent attempt of fine tuning *p*-type Bi₂Te₃ into the nonmetallic regime through elemental Tl doping. We provide transport property measurements from 2 to 300 K that reveal interesting physical phenomena in Tl-doped Bi₂Te₃ single crystals as the position of the Fermi level is being altered.

II. EXPERIMENT

Single crystals of Bi₂Te₃ containing Tl with the nominal concentration corresponding to Bi_{2-x}Tl_xTe₃, $0 \leq x \leq 0.30$, were synthesized using a modified Bridgman method. First, we prepared Tl₂Te₃ from stoichiometric quantities of Tl and Te weighted under argon and then added appropriate amounts of Bi and Te. All elements were of 5N purity. The synthesis was done in well-evacuated quartz ampoules with a tapered bottom. After annealing at 1090 K for 24 h, single crystals were grown via lowering ampoules through a temperature gradient of 400 K/5 cm at a rate of 4.5 mm/hour. The resulting single crystals were easily cleavable along the hexagonal (0001) planes, i.e., perpendicular to the trigonal *c* axis.

Powder x-ray diffraction (XRD) patterns (2θ , $10^\circ-80^\circ$) were characterized using a Scintag X1 x-ray diffractometer with Cu $K\alpha$ radiation on powders obtained by grinding central parts of the single crystals. A JEOL 3011 transmission electron microscope (TEM) operating at 300 kV was used to analyze the detailed microstructure. The chemical composition analysis was conducted using energy dispersive spectrometry (EDS). The TEM specimen was prepared by *in situ* focused ion beam (FIB) lift-out method, performed in an FEI Helios 650 workstation. To study the chemical states, x-ray

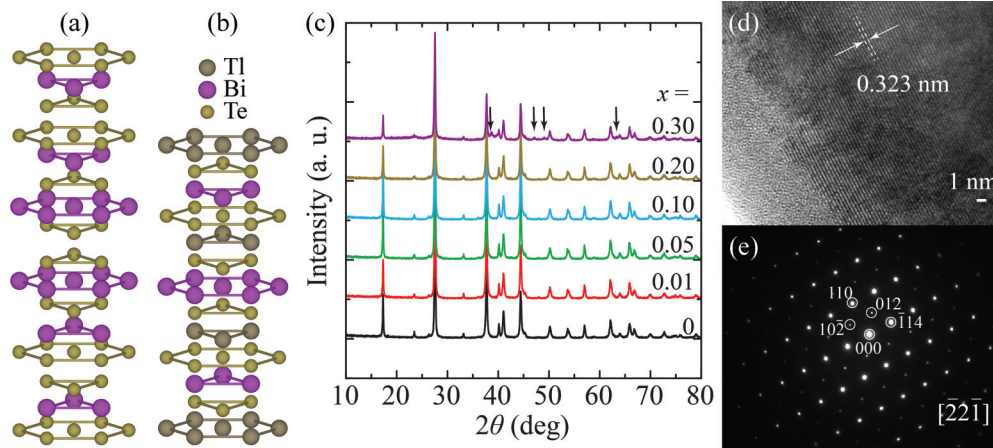


FIG. 1. (Color online) Crystal structure of (a) Bi_2Te_3 and (b) TlBiTe_2 with repeating $(\text{Te}^1\text{-Bi-Te}^2\text{-Bi-Te}^1)$ and (Te-Bi-Te-Tl) layers, respectively. Defected form of TlBiTe_2 represented by $(\text{Te-Bi-Te-Tl-V}_{\text{Te}}^{\bullet\bullet}) + 2e$ includes an atomic plane of Te vacancies, has nearly identical lattice parameters as Bi_2Te_3 , shares the same space group, and donates electrons necessary to explain transport properties. (c) XRD patterns of powders made from Tl-doped Bi_2Te_3 single crystals, matching the Bi_2Te_3 standard (JCPDS 82-0358), with arrows indicating additional peaks of the TlBiTe_2 phase, which is also confirmed by (d) HRTEM image and (e) SAED pattern taken from the $x = 0.30$ sample. The distance of the neighboring lattice fringes in (d) is 0.323 nm, in agreement with the $(\bar{1}14)$ lattice spacing for TlBiTe_2 .

photoelectron spectroscopy (XPS) investigation was performed in a Kratos Axis Ultra XPS system using a monochromatic Al source, where Cu was adopted as the binding-energy reference.

Samples with dimensions $10 \times 3 \times 2 \text{ mm}^3$ (2 mm along the trigonal c axis) for physical property characterizations were cut from the central part of the single crystals with a spark erosion machine. Low-temperature transport property measurements were carried out over the temperature range of 2–300 K. Electrical resistivity, Seebeck coefficient, and thermal conductivity were determined using a longitudinal steady-state technique in a homemade cryostat. Thermal gradients were measured by fine Chromel-Au/Fe thermocouples, with a small strain gauge serving as the heat source. As Seebeck probes we used fine copper wires carefully calibrated to correct for the absolute thermopower of Cu.¹⁰ Galvanomagnetic measurements were carried out in a Quantum Design MPMS system (magnetic field up to 5.5 T), using a Linear Research ac bridge with 16-Hz excitation. The current was in the (0001) plane for all transport measurements, while the magnetic field for Hall measurements was oriented parallel to the c axis. The uncertainties of electrical resistivity, Seebeck coefficient, and thermal conductivity are estimated to be $\pm 3\%$, $\pm 3\%$, and $\pm 7\%$, respectively.

III. RESULTS

As shown in Fig. 1(a), Bi_2Te_3 has a layered structure formed by $(\text{Te}^1\text{-Bi-Te}^2\text{-Bi-Te}^1)$ type of quintuple layers (QLs), often referred to as the tetradymite-type lattice. The XRD patterns in Fig. 1(c) suggest all samples can be readily indexed to the Bi_2Te_3 phase (JCPDS 82-0358),¹¹ with additional peaks (indicated by arrows) in the $x = 0.30$ sample that can be ascribed to the formation of rhombohedral TlBiTe_2 phase (JCPDS 85-0421).¹² Figures 1(d) and 1(e) show the high-resolution transmission electron microscopy (HRTEM) image and selected area electron diffraction (SAED) pattern taken

from a TEM specimen prepared from the $x = 0.30$ crystal. The measured distance of the neighboring lattice fringes in Fig. 1(d) is 0.323 nm, in agreement with the $(\bar{1}14)$ lattice spacing for TlBiTe_2 . The EDS analysis on the specimen indicates it contains 23.7 at.% Tl, 22.3 at.% Bi, and 54.0 at.% Te, which verifies the chemical composition. The crystal structure of TlBiTe_2 , as shown in Fig. 1(b), is typified by (Te-Bi-Te-Tl) type of layers and recently noted as a new family of TI.¹³

Incorporation of Tl into the tetradymite-type lattice of Bi_2Te_3 deserves a comment. One might naively expect the atoms of Tl to substitute for Bi. This to be the case, such doping would enhance the density of holes. As we shall see later, this is contrary to the experimental results that clearly show a crossover from p -type to n -type dominated transport as the content of Tl increases. A simple scenario in which Tl occupies interstitial sites or is in the van der Waals gap of the Bi_2Te_3 structure is also unlikely as this contradicts no changes being observed in the lattice parameters. Finally, arguing that the presence of Tl increases the bond polarity and thus decreases the probability of formation of antisite defects Bi_{Te} that give bulk Bi_2Te_3 its p -type character, is also unlikely as the content of Tl is very low in these studies. In fact, as the above structural and compositional analysis using XRD, HRTEM, and SAED indicates, it is via the formation of TlBiTe_2 how Tl enters the Bi_2Te_3 lattice. This mechanism was originally suggested in Ref. 14 and we now have an experimental proof of its existence. Since Bi_2Te_3 and TlBiTe_2 are closely related (the same D_{3d}^5 space group and nearly identical parameters of the TeBi_6 octahedra forming both Bi_2Te_3 and TlBiTe_2), there is only small energy penalty to be paid by replacing a quintuple layer of $(\text{Te}^1\text{-Bi-Te}^2\text{-Bi-Te}^1)$ by a defected stack of $(\text{Te-Bi-Te-Tl-V}_{\text{Te}}^{\bullet\bullet}) + 2e$, where $\text{V}_{\text{Te}}^{\bullet\bullet}$ represents an atomic plane of Te vacancies. Patches of such empty Te planes will be randomly distributed among the neighboring Te^1 sites without forming a continuous layer of unoccupied sites. The most important, the symbiosis of the two structures provides means for supplying electrons in Bi_2Te_3 which then compensate holes

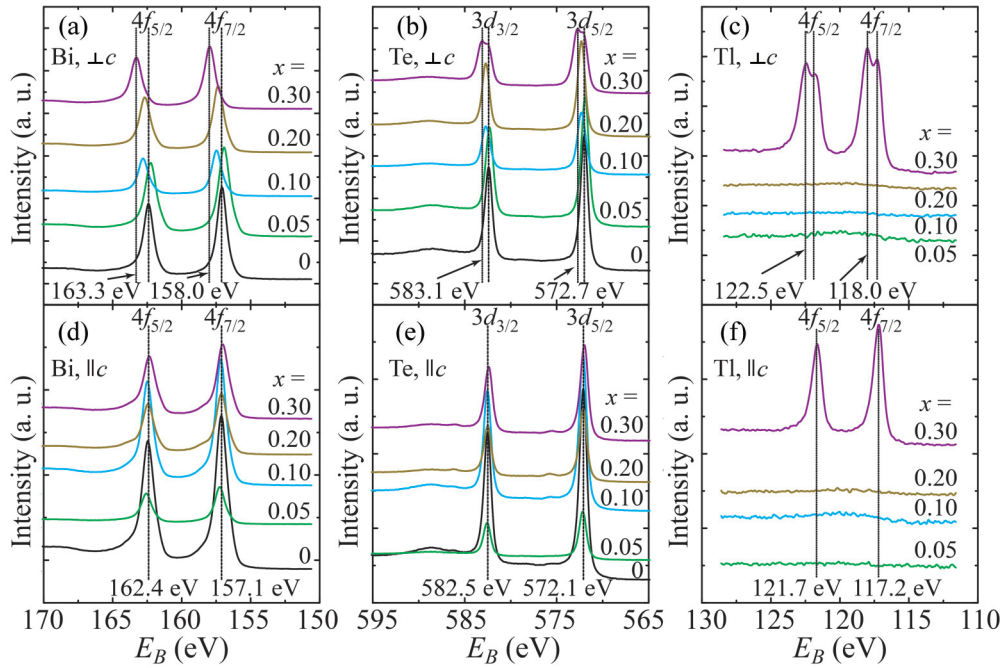


FIG. 2. (Color online) XPS analysis performed on various TI-doped Bi_2Te_3 surfaces either perpendicular to the c axis ($\perp c$, i.e. the basal plane) or parallel to the c axis ($\parallel c$) showing core levels for (a) Bi $4f$, $\perp c$; (b) Te $3d$, $\perp c$; (c) Tl $4f$, $\perp c$; (d) Bi $4f$, $\parallel c$; (e) Te $3d$, $\parallel c$; (f) Tl $4f$, $\parallel c$.

and, with the increasing content of TI, eventually take over and dominate the transport, as shown below.

Figure 2 presents the XPS signals for Bi $4f$ [Figs. 2(a) and 2(d)], Te $3d$ [Figs. 2(b) and 2(e)], and Tl $4f$ [Figs. 2(c) and 2(f)] core levels of various TI-doped Bi_2Te_3 samples, collected from freshly prepared surfaces either perpendicular to the c axis ($\perp c$, i.e., the basal plane) or parallel to the c axis ($\parallel c$), where carbon and oxygen contamination was removed via Ar ion sputtering. The XPS signal was picked up from an analyzed area of approximately ~ 1.5 mm in diameter. The layered nature of Bi_2Te_3 matters in XPS to the extent that the signal from the $\parallel c$ surface (where incident x rays encounter a cross section of multiple QLs and everything in-between) should be more informative than that from the $\perp c$ surface (where incident x rays see a plane of QLs), in studying the chemical environment between QLs.

For sample $x = 0$, the binding energies E_B of Bi and Te determined from both $\perp c$ [Bi, Fig. 2(a); Te, Fig. 2(b)] and $\parallel c$ [Bi, Fig. 2(d); Te, Fig. 2(e)] surfaces are identical and agree with the literature values for Bi_2Te_3 ,¹⁵ as summarized in Table I. As shown in Figs. 2(a) and 2(b), when x increases

TABLE I. Binding energies E_B in eV observed by XPS.

	Bi		Te		Tl	
	$4f_{5/2}$	$4f_{7/2}$	$3d_{3/2}$	$3d_{5/2}$	$4f_{5/2}$	$4f_{7/2}$
Bi_2Te_3^a	162.5	157.2	582.3	572.0		
Tl ^b					122.17	117.73
$x = 0$	162.4	157.1	582.5	572.1		
$x = 0.30$	163.3	158.0	583.1	572.7	122.5,	118.0,
					121.7	117.2

^aFrom Ref. 15.

^bFrom Ref. 16.

from 0 to 0.30, the Bi and Te peaks obtained from the $\perp c$ surface systematically shift toward higher energy, which we interpret as a change of the valence state in Bi and Te due to TI presence in the lattice. The existence of TI in the crystal is confirmed by the emergence of peaks corresponding to the Tl $4f$ levels in sample $x = 0.30$ as illustrated in Fig. 2(c), which are listed in Table I and compared with literature values for pure Tl.¹⁶ The atomic concentration for TI is estimated to be $3.83 \pm 1.95\%$, somewhat lower than the nominal value 6% for $x = 0.30$. However, the XPS spectra of sample $x = 0.30$ in the $\perp c$ surface differ from that in the $\parallel c$ surface. Since the Bi and Te $\parallel c$ peaks of the sample $x = 0.30$ do not deviate from that of the sample $x = 0$, as shown in Figs. 2(d) and 2(e), we ascribe the Tl $\parallel c$ peaks of sample $x = 0.30$ in Fig. 2(f) to some loosely bonded TI atoms which leave the binding energies of Bi and Te essentially unchanged. Even though TI peaks were indeed observed in the XPS survey scan of sample $x = 0.20$, no discernible TI signal in the XPS core scan was picked up for samples with $x \leq 0.20$ (even after several attempts), probably due to the very low concentration of TI actually incorporated in the crystals (amounts much lower than one would expect based on the nominal x), together with the uneven distribution of TI in the crystal (we have observed a large standard deviation of TI concentration in the sample of $x = 0.30$). There is no doubt that TI reveals its presence in Bi_2Te_3 on transport properties of the crystals, but it is difficult to establish its presence quantitatively by whatever analytical measurement.

The temperature-dependent electrical resistivity ρ and Seebeck coefficient S measured in the (0001) plane are shown in Figs. 3(a) and 3(b), respectively. The pure Bi_2Te_3 ($x = 0$) exhibits a metallic electrical resistivity behavior ($\rho_{300\text{K}} = 14.0 \mu\Omega \text{ m}$) and shows a positive Seebeck coefficient ($S_{300\text{K}} = +245 \mu\text{V K}^{-1}$) in the entire temperature range covered. This p -type stoichiometric Bi_2Te_3 thus behaves as a highly

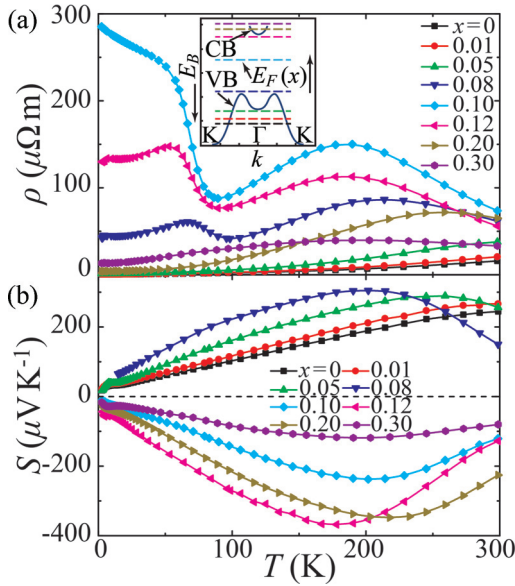


FIG. 3. (Color online) Temperature-dependent (a) electrical resistivity ρ and (b) Seebeck coefficient S for TI-doped Bi_2Te_3 single crystals. The inset in (a) is a sketch of the band structure (binding energy E_B vs wave vector k) along the Γ -K direction, where Fermi level E_F for various x are indicated by horizontal dashed lines. With increasing amount of TI, the E_F is shifted continuously from the valence band (VB) into the conduction band (CB).

degenerate semiconductor with the hole concentration $n_{300\text{K}} = +1.12 \times 10^{19} \text{ cm}^{-3}$ [see Fig. 4(b), where positive (negative) n indicates hole (electron)]. The Fermi level E_F , in this case, lies in the valence band (VB). With the increasing content of TI, as shown below, E_F continuously shifts out of VB into the band gap and towards the edge of the conduction band (CB). A sketch of the band model along the Γ -K direction,^{9,17,18} together with the position of E_F (dashed lines) corresponding to various x values, is presented as the inset of Fig. 3(a). By properly choosing the content of TI ($0.08 \leq x \leq 0.12$), one can pin E_F in the band gap, a situation that is potentially favorable for the studies of TIs.

Upon increasing the content of TI up to $x = 0.05$, the system maintains its metallic conduction characteristics. However, a gradually decreasing density of holes, as shown in Fig. 4(b), leads to an increase in the electrical resistivity. This corresponds to a shift of E_F toward the VB maximum. Since the density of extrinsic carriers in these lightly TI-doped samples is decreased, the presence of thermal excitations across the band gap becomes evident on ρ versus T curves before room temperature is reached. Even clearer evidence of intrinsic excitations is seen in the behavior of the Seebeck coefficient where down-turns set in at progressively lower temperatures and are more dramatic as electrons start to compensate extrinsic holes.

Heavier TI content with x between 0.08 and 0.12 drives the system into a prominent nonmetallic regime of conduction. During this transition, the density of extrinsic holes is greatly diminished, the carrier type changes from that of a hole-dominated to an electron-dominated transport [see the behavior of the Seebeck coefficient in Fig. 3(b), and the Hall coefficient in Fig. 4(a)], and E_F shifts from a position

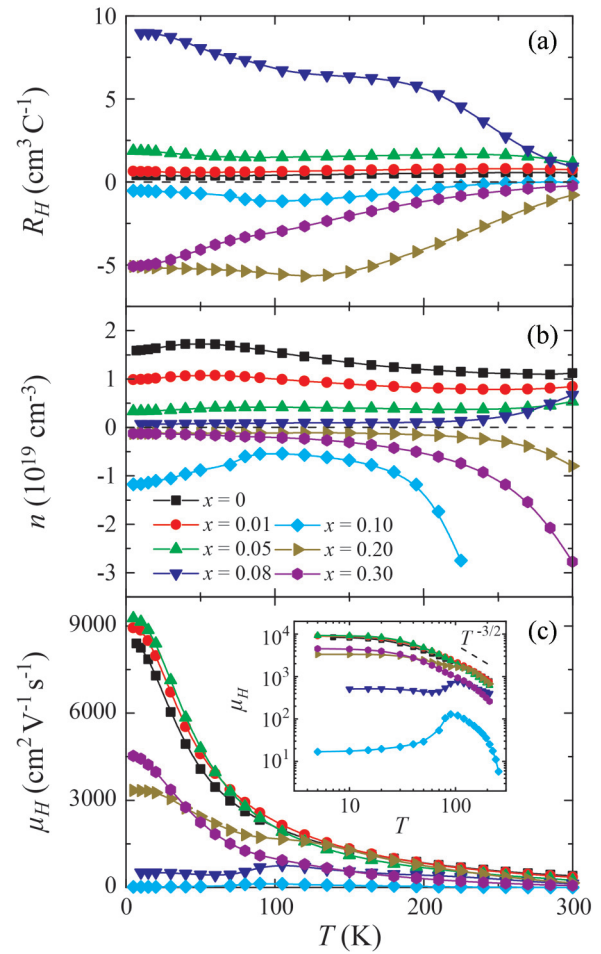


FIG. 4. (Color online) Temperature-dependent (a) Hall coefficients R_H from 2 to 300 K, (b) carrier density defined as $n = 1/(e R_H)$, where e is the elementary charge and positive (negative) n stands for hole (electron), and (c) Hall mobility defined as $\mu_H = R_H/\rho$. Note that such definitions are only feasible for temperatures up to ~ 200 K where one can assume the dominance of a single carrier in the transport of TI-doped Bi_2Te_3 single crystals. The inset in (c) is μ_H vs T plotted on a log-log scale indicating the $T^{-3/2}$ acoustic phonon temperature dependence at temperatures near the ambient.

close to the top of VB ($x = 0.08$) to a location deep into the band gap ($x = 0.10$), and then approaches the bottom of CB ($x = 0.12$). Very low background carrier concentrations of samples with $0.08 \leq x \leq 0.12$ make thermal excitations across the band gap much more prominent in both the resistivity and Seebeck coefficient data and bipolar contributions are manifested at even lower temperature ~ 200 K. Interestingly, when the TI-doped Bi_2Te_3 crystals ($x = 0.08$ – 0.12) are cooled down from ~ 200 K, a metal-insulator type of transition at ~ 100 K is always observed in ρ . Below ~ 100 K, the system displays a distinctly insulating behavior (rather than metallic) corresponding to the Fermi level being buried in the band gap. Surprisingly, the insulating behavior peaks near 50 K and is followed by a decreasing resistivity (samples $x = 0.08$ and 0.12) or a tendency to quasisaturate ($x = 0.10$) that persists down to the lowest temperatures of the experiment. Such unique metallic conduction below ~ 50 K in the case of $0.08 \leq x \leq 0.12$ could be a manifestation of the dominance

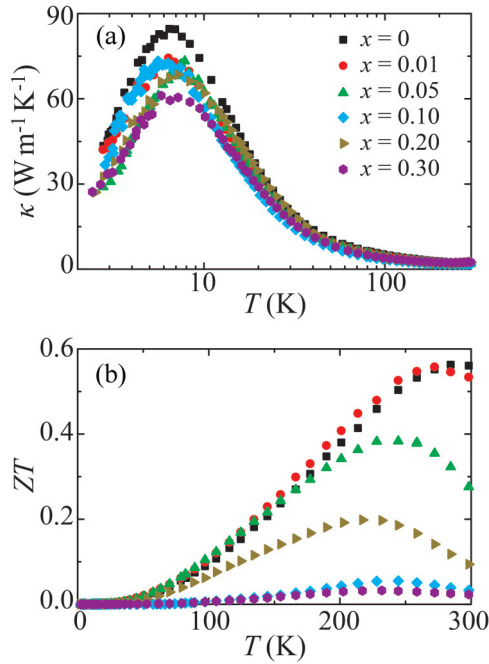


FIG. 5. (Color online) The temperature dependence of (a) thermal conductivity κ for TI-doped Bi_2Te_3 single crystals, and (b) the resulting thermoelectric figure of merit ZT .

of the surface metallic state. However, why the metallic state abruptly ceases to exist near 50 K, the gap opens, and the insulating state takes over is an open question. It is worth noting that a similar transport response was also observed in TI-doped PbTe ,¹⁹ where the resonant states introduced by TI are believed to play an important role in understanding such effect.

The behavior described above regarding ρ maps well onto the trend observed in S . In the regime dominated by extrinsic holes ($0 \leq x \leq 0.08$), as ρ increases, the positive S increases. Likewise, in the regime where ρ is governed by electrons ($x = 0.12-0.30$), a decreasing ρ leads to a decreasing magnitude of the negative S . We also note that a local maximum is seen in the magnitude of S near ~ 7 K for all samples regardless of TI-doping level. This is likely a manifestation of the phonon-drag effect²⁰ reflecting a strong electron-phonon interaction at low temperatures and high-crystalline quality samples.

Results of the Hall coefficient (R_H) measurements are shown in Fig. 4(a), together with the carrier density n [defined as $n = 1/(e R_H)$] and applicable for a single parabolic band approximation, where e is the elementary charge, and positive (negative) n stands for holes (electrons)] and Hall mobility (defined as $\mu_H = R_H/\rho$) in Figs. 4(b) and 4(c), respectively. Note that, above ~ 200 K, where intrinsic excitations start to take place, such simplified experimental determination of the carrier density and mobility is no longer appropriate (see the unphysical sharp turns in n at high temperature for $x > 0.08$). This is also the reason why the $x = 0.10$ sample

shows “falsely” large carrier concentration which becomes even more significant at high temperatures since electrons and holes are compensating each other. We observe systematically varying carrier concentration for $x = 0-0.08$, where extrinsic holes dominate the transport process, resulting in positive R_H with density of holes suppressed as x increases. For $x = 0.20-0.30$, the negative R_H validates the electron-dominated conduction, where larger x tends to increase the density of electrons as the Fermi level moves deeper into the conduction band. Such tuning of carrier density is in accordance with the increasing content of TlBiTe_2 and therefore progressively higher density of electrons as the nominal amount x of TI increases. As shown in Fig. 4(c), carriers are clearly classified into three different categories: for $x = 0-0.05$, the mobility is high ($\mu_{10\text{K}} \sim 9000 \text{ cm}^2 \text{ V}^{-1} \text{ s}^{-1}$), while it becomes significantly suppressed (by a factor of ~ 16) to a low value ($\mu_{10\text{K}} \sim 560 \text{ cm}^2 \text{ V}^{-1} \text{ s}^{-1}$) for $x = 0.08$; with a further increase in TI content ($x = 0.20-0.30$), the crystal becomes an n -type conductor with μ_H restored to intermediate values ($\mu_{10\text{K}} \sim 3000-4000 \text{ cm}^2 \text{ V}^{-1} \text{ s}^{-1}$). The inset of Fig. 4(c) displays a log-log plot of μ_H versus T , indicating a temperature dependence of $\mu_H \sim T^{-3/2}$ that suggests the acoustic phonon scattering is playing an important role at temperatures near the ambient.

The temperature-dependent thermal conductivity κ of these TI-doped Bi_2Te_3 samples is shown in Fig. 5(a). The resulting dimensionless thermoelectric figure of merit $ZT = S^2\sigma T/\kappa$ is plotted in Fig. 5(b), indicating that a trace amount ($x \sim 0.01$) of TI may actually help to improve the thermoelectric performance of Bi_2Te_3 . Higher concentrations of TI have a clearly negative impact on the thermoelectric performance. The total thermal conductivity can be decomposed as $\kappa = \kappa_L + \kappa_e$, where κ_L and κ_e are the lattice and electronic thermal conductivities, respectively. The κ_L is calculated by subtracting κ_e obtained from the Wiedemann-Franz law. Here, $\kappa_e = L\sigma T$, where $\sigma (= 1/\rho)$ is the electrical conductivity and L is the Lorenz number. Note that under the single parabolic band approximation with one dominant carrier type,¹ the Seebeck coefficient is given by

$$S = -\frac{k_B}{q} \left[\eta - \frac{(r+5/2)F_{r+3/2}(\eta)}{(r+3/2)F_{r+1/2}(\eta)} \right], \quad (1)$$

where k_B is the Boltzmann constant, q is the charge of carrier [$+e$ ($-e$) for hole (electron)], r is the scattering index in the energy-dependent relaxation time $\tau = \tau_0 e^r$ (taken to be $-1/2$ for acoustic phonon scattering), $\eta = E_F/k_B T$ is the reduced Fermi level, and $F_n(\eta)$ is the n th Fermi-Dirac integral defined as

$$F_n(\eta) = \int_0^\infty \frac{\xi^n}{e^{\xi-\eta} + 1} d\xi. \quad (2)$$

Using η determined from the experimental values of Seebeck coefficient, the Lorenz number L can be estimated via

$$L = \frac{k_B^2}{q^2} \left[\frac{(r+3/2)(r+7/2)F_{r+1/2}(\eta)F_{r+5/2}(\eta) - (r+5/2)^2 F_{r+3/2}(\eta)^2}{(r+3/2)^2 F_{r+1/2}(\eta)^2} \right]. \quad (3)$$

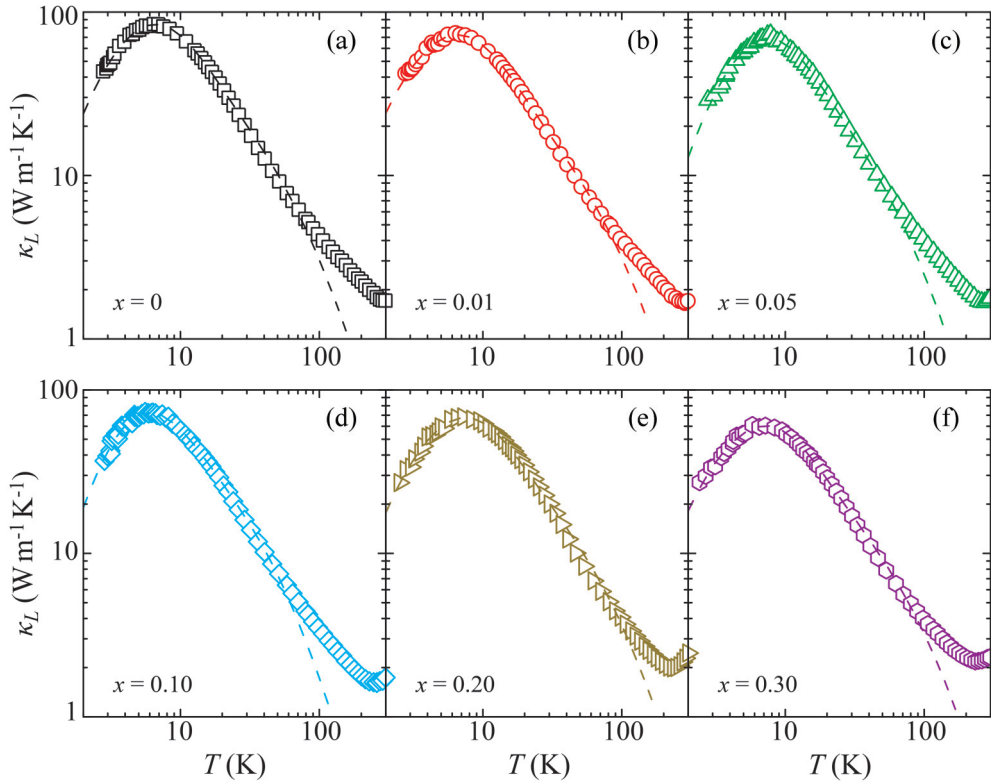


FIG. 6. (Color online) The lattice thermal conductivity κ_L of Tl-doped Bi_2Te_3 single crystals, with the dashed line indicating the numerical fitting result of the Debye-Callaway model for (a) $x = 0$, (b) $x = 0.01$, (c) $x = 0.05$, (d) $x = 0.10$, (e) $x = 0.20$, and (f) $x = 0.30$, which documents a generally enhanced point-defect scattering of phonons upon increasing the content of Tl.

The resulting T -dependent phonon conductivity κ_L is examined using the Debye-Callaway model^{21,22}

$$\kappa_L = \frac{k_B}{2\pi^2 v} \left(\frac{k_B}{\hbar} \right)^3 T^3 \int_0^{\theta_D/T} \frac{\tau_c x^4 e^x}{(e^x - 1)^2} dx, \quad (4)$$

where $x = \hbar\omega/k_B T$, ω is the phonon frequency, \hbar is the Planck constant, k_B is the Boltzmann constant, v is the averaged velocity of sound, θ_D is the Debye temperature, and τ_c is the relaxation time. The overall relaxation rate τ_c^{-1} is given by

$$\tau_c^{-1} = v/\ell + A\omega^4 + B\omega^2 T \exp(-\theta_D/3T) + C\omega T^3, \quad (5)$$

where terms on the right-hand side correspond to the boundary scattering (ℓ is the mean grain size), defect scattering, umklapp processes,²³ and normal scattering,²⁴ respectively. Here, ℓ , A , B , and C are fitting parameters. Figure 6 presents the lattice thermal conductivity for various Tl-doped Bi_2Te_3 single

crystals. The dashed lines are the numerical fitting result of Eqs. (4) and (5), with $v = 2.0$ km/s,²⁵ and $\theta_D = 165$ K.²⁶ Fitting parameters are listed in Table II. Such model depicts the temperature dependence of κ_L very well at low temperatures, but starts to underestimate κ_L for $T > 100$ K, where effects of radiation loss, temperature dependence of Lorenz number, and bipolar thermal conductivity all contribute. An attempt to include electron-phonon scattering (e.g., $\tau_{e-p}^{-1} \sim \omega^2$) in the calculations did not improve the overall fit. Note that the increasing content of Tl generally leads to a lower dielectric maximum in κ_L , a broader peak, and its slight shift to higher temperatures, with an enhanced strength of point-defect scattering of phonons.

IV. CONCLUSION

While it is difficult to establish quantitatively (and even qualitatively at low Tl concentrations) the presence of Tl in the crystal lattice of Bi_2Te_3 , its systematic effect on the transport behavior leaves no doubt that Tl plays an important role in shifting the Fermi level and thus transport properties of Bi_2Te_3 . The incorporation of Tl in Bi_2Te_3 proceeds via the formation of defected layers of TlBiTe_2 that contain charged vacant planes of Te. Such structure is crystallographically akin to Bi_2Te_3 and seems randomly distributed. Moreover, it is the source of electrons responsible for an effective way of tuning p -type metallic Bi_2Te_3 gradually into an n -type conductor with the increasing content of Tl, and therefore TlBiTe_2 , as confirmed by measurements of the Seebeck coefficient and the

TABLE II. Lattice thermal conductivity fitting parameters for Tl-doped Bi_2Te_3 single crystals, as defined by Eq. (5)

x	ℓ (mm)	A (10^{-42} s ³)	B (10^{-17} s K ⁻¹)	C (10^{-8} K ⁻³)
0	0.488	1.036	0.944	1.358
0.01	0.593	1.765	1.018	1.078
0.05	0.215	0.851	1.209	1.738
0.10	0.321	0.530	0.952	3.275
0.20	0.382	1.703	0.746	0.968
0.30	0.441	2.251	0.870	1.009

Hall effect. During the p - n transition, interesting nonmetallic states are present with unique electrical resistivity profile. Samples having the Fermi level in the band gap display a metallic or quasisaturated conduction below ~ 50 K. This might be a transport signature of the presence and dominance of the topologically protected surface state. Introducing Tl into the crystal lattice of Bi_2Te_3 thus might be of interest in achieving bulk insulating states that then allow detection of surface states. Thermal conductivity of Tl-doped Bi_2Te_3 is suppressed on account of enhanced point-defect scattering.

Very low concentrations of Tl seem to marginally improve the thermoelectric performance of Bi_2Te_3 .

ACKNOWLEDGMENTS

This work was supported as part of the Center for Solar and Thermal Energy Conversion, an Energy Frontier Research Center funded by the US Department of Energy, Office of Science, Basic Energy Sciences under Award No. DE-SC-0000957.

*Corresponding author: cuher@umich.edu

- ¹H. J. Goldsmid, *Electronic Refrigeration* (Pion, London, 1986).
- ²H. Zhang, C.-X. Liu, X.-L. Qi, X. Dai, Z. Fang, and S.-C. Zhang, *Nat. Phys.* **5**, 438 (2009).
- ³Y. L. Chen, J. G. Analytis, J.-H. Chu, Z. K. Liu, S.-K. Mo, X. L. Qi, H. J. Zhang, D. H. Lu, X. Dai, Z. Fang, S. C. Zhang, I. R. Fisher, Z. Hussain, and Z.-X. Shen, *Science* **325**, 178 (2009).
- ⁴D. Hsieh, Y. Xia, D. Qian, L. Wray, J. H. Dil, F. Meier, J. Osterwalder, L. Patthey, J. G. Checkelsky, N. P. Ong, A. V. Fedorov, H. Lin, A. Bansil, D. Grauer, Y. S. Hor, R. J. Cava, and M. Z. Hasan, *Nature* **460**, 1101 (2009).
- ⁵Y. Xia, D. Qian, D. Hsieh, L. Wray, A. Pal, H. Lin, A. Bansil, D. Grauer, Y. S. Hor, R. J. Cava, and M. Z. Hasan, *Nat. Phys.* **5**, 398 (2009).
- ⁶Y. L. Chen, J.-H. Chu, J. G. Analytis, Z. K. Liu, K. Igarashi, H.-H. Kuo, X. L. Qi, S. K. Mo, R. G. Moore, D. H. Lu, M. Hashimoto, T. Sasagawa, S. C. Zhang, I. R. Fisher, Z. Hussain, and Z. X. Shen, *Science* **329**, 659 (2010).
- ⁷C. B. Satterthwaite and R. W. Ure, Jr., *Phys. Rev.* **108**, 1164 (1957).
- ⁸Y. S. Hor, D. Qu, N. P. Ong, and R. J. Cava, *J. Phys.: Condens. Matter* **22**, 375801 (2010).
- ⁹Y. S. Hor, J. G. Checkelsky, D. Qu, N. P. Ong, and R. J. Cava, *J. Phys. Chem. Solids* **72**, 572 (2011).
- ¹⁰C. Uher, *J. Appl. Phys.* **62**, 4636 (1987).
- ¹¹Y. Feutelais, B. Legendre, N. Rodier, and V. Agafonov, *Mater. Res. Bull.* **28**, 591 (1993).
- ¹²E. F. Hockings and J. G. White, *Acta Crystallogr.* **14**, 328 (1961).
- ¹³Y. L. Chen, Z. K. Liu, J. G. Analytis, J. H. Chu, H. J. Zhang, B. H. Yan, S. K. Mo, R. G. Moore, D. H. Lu, I. R. Fisher, S. C. Zhang, Z. Hussain, and Z. X. Shen, *Phys. Rev. Lett.* **105**, 266401 (2010).
- ¹⁴P. Lošćák, P. Bezdička, J. Horák, and J. Šrámková, *Radiat. Eff. Defects Solids* **138**, 251 (1996).
- ¹⁵H. Bando, K. Koizumi, Y. Oikawa, K. Daikohara, V. A. Kulbachinskii, and H. Ozaki, *J. Phys.: Condens. Matter* **12**, 5607 (2000).
- ¹⁶N. Martensson, A. Berndtsson, and R. Nyholm, *J. Electron. Spectrosc.* **19**, 299 (1980).
- ¹⁷D.-X. Qu, Y. S. Hor, J. Xiong, R. J. Cava, and N. P. Ong, *Science* **329**, 821 (2010).
- ¹⁸J. Zhang, C.-Z. Chang, Z. Zhang, J. Wen, X. Feng, K. Li, M. Liu, K. He, L. Wang, X. Chen, Q.-K. Xue, X. Ma, and Y. Wang, *Nat. Commun.* **2**, 574 (2011).
- ¹⁹J. P. Heremans, V. Jovovic, E. S. Toberer, A. Saramat, K. Kurosaki, A. Charoenphakdee, S. Yamanaka, and G. J. Snyder, *Science* **321**, 554 (2008).
- ²⁰C. Herring, *Phys. Rev.* **96**, 1163 (1954).
- ²¹J. Yang, G. P. Meisner, D. T. Morelli, and C. Uher, *Phys. Rev. B* **63**, 014410 (2000).
- ²²D. T. Morelli, J. P. Heremans, and G. A. Slack, *Phys. Rev. B* **66**, 195304 (2002).
- ²³C. J. Glassbrenner and G. A. Slack, *Phys. Rev.* **134**, A1058 (1964).
- ²⁴R. Berman and J. C. F. Brock, *Proc. R. Soc. London, Ser. A* **289**, 46 (1965).
- ²⁵J. O. Jenkins, J. A. Rayne, and R. W. Ure, Jr., *Phys. Rev. B* **5**, 3171 (1972).
- ²⁶G. E. Shoemaker, J. A. Rayne, and R. W. Ure, Jr., *Phys. Rev.* **185**, 1046 (1969).